Effects of Si Slabs on the Performance of CdO Thin Films Designed for Optoelectronic Applications

Sabah E. AlGarni[a], A.F. Qasrawi[b,c*] (iD)

[a]*University of Jeddah, Faculty of Science, Department of Physics, Jeddah, Saudi Arabia.*
[b]*Arab American University, Department of physics, Jenin 240, Palestine.*
[c]*Istinye University, Department of Electrical and Electronics Engineering, 34010, Istanbul, Turkey.*

Herein, the structural, morphological, optical and electrical properties of CdO stacked layers comprising Si slabs of thickness of 100 nm are investigated. The performance of the stacked layers, which are prepared by the thermal evaporation technique under vacuum pressure of 10^{-5} mbar, is remarkably enhanced via insertion of Si thin slabs. The presence of Si slabs between the layers of CdO improves the crystallinity and surface morphology, increases the light absorbability in the ultraviolet and visible ranges of light and also increases the dielectric constant, the quality factor, and optical conductivity values. The optical conductivity parameters, which are analyzed in accordance with Drude-Lorentz approach, have shown that the insertion of the Si layers rises the values of the drift mobility of holes in CdO and lowers the free holes concentration. The energy band gap of CdO films is narrowed from 2.20 to 1.27 eV upon insertion of Si slabs. The applicability of the plasmonic CdO/Si/CdO devices as low pass filers in the frequency domain of 0.01-1.80 GHz is verified through impedance spectroscopy measurements.

Keywords: *CdO/Si/CdO, high absorbance, optical conductivity, microwave cavity.*

1. Introduction

Thin film devices has attracted the attention owing to the novel performance they reveal. As for examples, integrating CdS/CdTe P-N thin-film diodes with poly-Si thin-film transistors in an active pixel sensor scheme is found suitable for a wide range of applications including X-ray imagers, gamma-ray detectors, and thermal neutron detectors[1]. In addition, nanostructured III–V semiconductor quantum wells, quantum wires, and quantum dots are mentioned playing vital role in enhancing the performance of solar cells[2]. Moreover, it is also reported that future computational imaging systems is to include a series of deep and flat optical layers that need to be easily stackable and exhibit sets of very demanding linear, nonlocal and nonlinear optical properties[3].

Due to the large surface area to the volume ratio of layered structured materials, the surface engineering of these structures seems to be one of the most important challenges that occupy the interest of researchers while finding applications for such structures. One of the engineering methods is the laser assisted texturing[4]. The resulting textures are found to exhibit remarkable crystal structures and high contrast of surface properties on a nanoscale level[4]. Alternatively, zinc(II)- coordinated nanostructured polymers are reported to have photocatalytic activity for the degradation of organic dyes[5]. In addition, SnO_2 nanosheets that were synthesized using microwave hydrothermal method were found to be promising for use in Li-ion based batteries as an electrode material[6]. Furthermore, in-plane micro-supercapacitors that

have a high power density, and remarkable rate capability as well as long cycling stability were successfully produced by the nano-sandwiching of metal with hexacyanoferrate/graphene hybrid thin films[7]. In another work, the nanosandwiching of indium between two layers of copper oxide and gallium sulfide was able to engineer the energy band gap and to enhance the dielectric performance of the gallium sulfide thin films[8]. In the same context, insertion of YAu alloy of thickness of 140 nm between two layers of ZnSe[9] successfully increased the drift mobility in the ZnSe thin films from 1098 to 1766 cm^2/Vs. The plasmon frequency in ZnSe was also shifted from 0.94 to 2.13 GHz upon nanosandwiching. Consistently, Au nanosheets are also observed to alter the properties of ZnS films. It was reported that, the increase of Au layer thickness in the ZnS/Au/ZnS structure result in increased carrier concentration leading to decreased resistivity and in the declined transmittance in the visible light region[10].

The above mentioned enhancements in the properties of semiconductors that are achieved via the sandwiching technique motivated us to establish a new system of CdO sandwiched with thin layers of Si. Like other smart oxide materials[11], cadmium oxide thin films prepared by the sol–gel technique onto Si substrates are observed exhibiting cubic crystal structure and energy band gap value of 2.29 eV[12]. The Si/CdO films revealed high rectifying behavior and a strong photoresponse making it appropriate for fabrication of photodetectors operating in the UV/visible ranges of light[12]. In the same context, literature data showed highly promising results with the use of Si nanosheets in optoelectronics

technology. As an example, Si nanosheets prepared by plasma-doping technique are reported to be the key component of 2D electronics. They are also key components for spintronic, optics and sensing devices[13]. Another example is transistors that comprise Si nanosheets in their structure revealed fields effect hole mobility of 329 cm²/Vs and ON/OFF ratio of 10^6[13]. In addition, Si nanosheets are mentioned employable as an effective optical modulating device for a solid-state lasers[14]. Moreover, the superior electrochemical properties of Si nanosheets make them applicable as an electrode in lithium ion batteries[15]. Si nanosheets combined with graphene oxides assisted delivering high reversal capacity and current density[15]. In the light of the above mentioned improvements that are reached via Si nanosheets, here in this work we have carried out experiments using Si nanosheets to improve the structural and optical properties of CdO thin films. The novelty and aim of the current work appears in enhancing the optical conductivity parameters of CdO via Si nanosheets. Particularly, the role of Si sheets on the optical conductivity parameters presented by free charge carrier density, drift mobility, plasmon frequency and scattering time at femtosecond levels will be explored as they play vital role in the performance of optoelectronic devices. Some verifying examples of applicability as microwave filters will also be considered.

2. Experimental Details

Stacked layers of Si and CdO thin films are prepared by the thermal deposition techniques using VCM-600 vacuum coater. The thermal evaporation technique is relatively simple, fast and cost-effective for the preparation of stacked nano-layers like heterojunction devices[16] including solar cells. Thermal evaporation technique is the most suitable for physically stacked layers because it gives several advantages such as high stability, high reproducibility, high deposition rate, large area deposition, uniform and compact films which are very important properties for thin films[16]. Earlier surface morphology analysis on thin films has shown that the vacuum thermal evaporation technique is one of the most appropriate techniques for the production of nano-crystals based films[17]. The 500 nm thick CdO films were grown onto glass and Yb substrates at room temperature under vacuum pressure of 10^{-5} mbar during the evaporation cycle. The grown glass/CdO (500 nm) substrates and Yb/CdO films were employed to grow Si layers of thicknesses of 100 nm using the VCM-600 system. The resulting (glass, Yb)/CdO/Si films were then re-coated with another 500 nm thick CdO layer. For some of the samples, the third CdO layer was coated onto the (glass, Yb)/CdO films to form (glass, Yb)/CdO/CdO stacked layers. The top surface of the Yb/CdO/Si/CdO film were eventually masked and painted with point contact of areas of 3.14×10^{-2} cm^2 electrodes of Ag to allow ac signal propagation in the samples. The film thicknesses were measured with the help of an in situ INFICON STM-2 thickness monitor. The X-ray studies of the stacked layers were carried out by Miniflex 600 diffractometer. The scanning electron microscopy images were collected by COXEM 200 SEM system. The transmittance and reflectance spectra were measured via thermos-scientific evolution 300 spectrophotometer equipped with VEE MAX

II reflection accessory. The impedance spectra were recorded with the help of (10-1800 MHz) Agilent impedance analyzer.

It is worth to mentioning that the production of high quality CdO thin films using thermal evaporation technique is arduous, since it requires specific parameters. For this reason, the films were always tested by optical microscopes and by scanning electron microscopes during the preparation cycles to insure the production of the homogeneity of the films. The uniform thickness were also tested by profilometer to observe the surface roughness and thicknesses. The currently reported films were obtained at vacuum pressure less than 6.0 $\times 10^{-5}$ mbar and at evaporation rate of ~10 Å/s. The evaporation was actualized using tungsten flat heaters. The distance between the source and film was 10 cm.

3. Results and Discussion

3.1. Structural properties

The geometrical design of the two stacked layers of CdO comprising Si slabs of thicknesses of 100 nm is shown in inset-1 of Figure 1. In order to investigate the effect of the Si thin layers on the properties of CdO, the prepared samples were subjected to X-ray diffraction (XRD) technical analyses. Figure 1 displays the results of the XRD measurements. It is clear from the figure that the studied samples are polycrystalline in nature. The XRD patterns for the CdO/CdO (CC) stacked layers and for the CdO/Si/CdO (CSC) samples display four intensive peaks centered at diffraction angles $2\theta = 28.95^o$, 32.05^o, 34.90^o and 38.55^o indicating that no extra phases were formed upon Si sheets insertion. Indexing the observed diffraction peaks in accordance with the existing literature data (Crystallography Open Database COD NO: 1011096) indicates that both of the CC and CSC thin films are cubic in nature and exhibit lattice parameter of value of $a = 4.8335 Å$ and $4.828 Å$, respectively. The theoretical analysis of the experimental data with the help of "Crystdiff" software packages, which considered all possible structures revealed only two of all observed peaks (centered at $2\theta = 32.05^o$ and 38.55^o), are assigned to the cubic CdO. The best orientation of the planes of the cubic phase of CdO appear along the (111) direction. The other two peaks which are minor compared to the maximum peaks were assigned to the hexagonal phase of $Cd(OH)_2$ (JCPDS card, No. 31-0228)[18]. The weight percentage of the $Cd(OH)_2$ phase in the structure of CdO before the insertion of Si slabs is 34.28%. The weight percentage of this minor phase decreased to 27.39% in the CSC samples. The formation of this minor phase in the structure of CdO was not observed for one layer of CdO but only appeared when two layers were stacked. Although the peak of $Cd(OH)_2$ previously appeared in the XRD patterns of the chemically deposited cubic CdO thin films[19], it was not indexed to any structural phase. The appearance of the $Cd(OH)_2$ hexagonal phase in the stacked layers of CdO is possibly due to the interaction of the surface of the first CdO layer with air atmosphere during the supplying of CdO powders to the evaporation source prior to the growth of second CdO layer.

Recalling that the crystal structure of silicon is identified as the face-centered cubic lattice with the Fm3d space
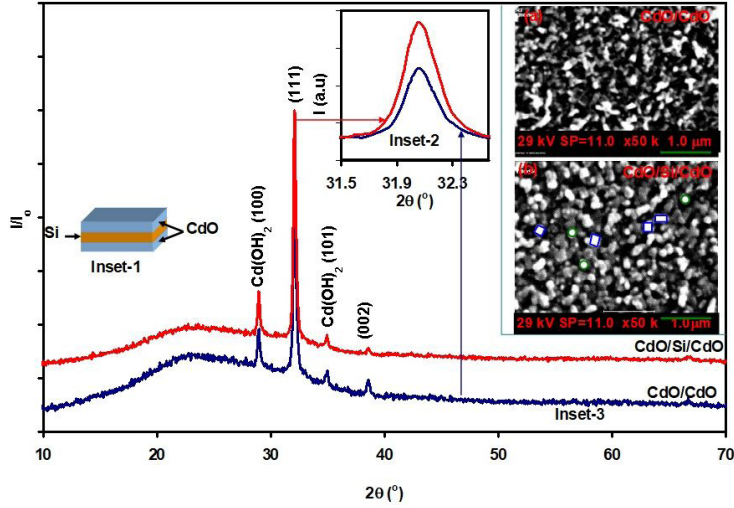
Figure 1. The X-ray diffraction patterns for CdO/CdO and CdO/Si/CdO films. Inset-1 shows the geometrical design of the studied samples, Inset-2 show the enlargement of the maximum peaks and inset-3 show the scanning electron microscopy images for the studied samples. The blue and green colored drawings show the shapes of the grains.

group and lattice constant $a = 5.43$ Å, then the lattice mismatches between CdO substrates and Si as epilayer is

$$\Delta\% = 100. \left| \frac{a_{CdO} - a_{Si}}{a_{Si}} \right| = 10.98\%^9.$$ Large lattice mismatches

between the layers results in high defect density which enables CdO/Si/CdO films to be used for producing a highly efficient light emitting diodes[9].

It is also clear from inset-2 of Figure 1 that the intensity of the maximum peak of CdO has increased significantly upon insertion of Si slabs. The peak intensity increased by 150%. The maximum peak of CdO in CSC samples become broader. Analysis of the structural parameters using the maximum peak broadening (β) with the help of the following equations[9],

$$\epsilon = \beta / (4 \tan(\theta)), \tag{1}$$

$$D = 0.94 \lambda / (\beta \cos(\theta)), \tag{2}$$

$$\delta = 15 \epsilon / (aD) \tag{3}$$

and

$$SF\% = 100 \cdot 2\pi^2 \beta / (45 \sqrt{3 \tan(\theta)}) \tag{4}$$

These equations allowed determining the structural parameters, where $\lambda = 1.5405$ Å, ϵ is the microstrain, D is the crystallite size, δ is the defect density and $SF\%$ is the stacking faults percentage. The calculated structural parameters of CC sample which are 3.64×10^{-3}, 36 nm, 3.14×10^{11} lines/cm^{-2} and 0.197% for ϵ, D, δ and $SF\%$ shifts to 4.02×10^{-3}, 33 nm, 3.83×10^{11} lines/cm^{-2} and 0.218%, respectively in CSC samples. The microstrain, the defect density and the stacking fault percentages increased by 10.4%, 4.96% and 10.56%, respectively, upon insertion of Si slabs between layers of CdO. The increase in the microstrain and other structural

parameters is ascribed to the local deviation of the Cd and O atoms from the equilibrium position in the crystalline lattice, owing to the presence of foreign Si impurities, porosities, point defects, dislocations or grain boundaries in the CdO samples.

Literature data reported that CdO usually exhibits Cd vacancies[20,21]. Since the ionic radius of Si[+4] being 0.56 Å is less than that of Cd[+2] (0.865 Å), occupation of Cd vacancies by Si atoms is highly preferable[22]. Si thin layers are also known to have large amount of dangling bonds on its surface[22]. As the bond length of Cd-O being 2.35 Å[23] is larger than that of Si-O (1.62 Å)[24], the columbic interactions at the interface between the two layers leads to the completeness of the broken bonds of Si through interaction with oxygen atoms. Such processes are also believed to be accompanied with slight stress which explains the increase in the strain, defect density and stacking faults upon Si slabs insertion[22]. Such studies take into an account that the effect of the Si doping on the properties of CdO that increases strain values with increasing doping concentration. This behavior is assigned to the differences in the ionic radii of Si[+4] and Cd[+2][25,26]. The author of that work assigned the structural variations to the occupation of interstitial locations in CdO lattice by Si ions[25,26].

One may also account the structural modifications to the interdiffusion process between Si and CdO layers. The interdiffusion is a process of diffusional exchange of atoms across two materials that are in contact. The process is driven by the chemical potential gradient across the boundaries that is observed in multilayers and nanocomposites due to the processing conditions. One of these conditions is the grain size reduction. In the nanoscale dimension, when grain size decreases, the atomic transport through grain boundaries becomes dominant over the volume diffusion leading to increased line shaped defects[27]. Our structural analyses have shown that with the reduction of the crystallite size from 36 to 33 nm, the defects density increases from

$3.14 \times 10^{11} lines / cm^2$ to $3.83 \times 10^{11} lines / cm^2$ upon interfacing of Si with CdO. The numerical data supports the belief of interdiffusion of Si in CdO.

Similar studies which are interested metal substitutions into oxides mentioned tha crystallite sizes of 37 nm are also achieved in CdO through doping with Al. The grain sizes are very large and could reach 500 nm[28]. In addition, doping ZnO with Mn mentioned that the crystallite size decreases due to the heavy doping content they mentioned that an amount of Mn ions higher than 2% can disturb the ZnO crystal lattice which brings to suppression of the crystal growth[29]. In another work CO doped ZnO exhibited a reduction in the crystallite size with increased doping content. The behavior was assigned to the lattice distortion or generation of the impurities or defects like oxygen deficiency[30]. In truth variation of crystallite sizes play main role in the optical and electrical properties. It is mentioned that the conduction band edges in materials are proportional to the inverse of grain diameter and becomes very large for a very small grain sizes[31].

3.2. Surface morphology

Inset-3 of Figure 1 illustrates the scanning electron microscopy images for the stacked layers of CdO before (inset-3 (a)) and after (inset-3 (b)) the insertion of Si slabs. Although the images are enlarged 50,000 times, the CC samples display irregularly shaped non-uniformly distributed grains. The grain sizes were evaluated using the software packages of the scanning electron microscope, which allows measuring sensitivity down to 1.0 nm. Some of the grains are rectangular and exhibit average grain size of 67 nm. Others are trapezoid shaped with average size of 117 nm. The samples which contain Si slabs in its structure exhibited more oriented circular and rectangular grains of average sizes of 70 nm. The grain sizes distribution changed in the range of 50~110 nm. As the grain is usually composed of

many crystallites, the enhancement in the grain sizes and the uniformity of the grains upon insertion of Si slabs is assigned to the more plane orientation along the (111) direction as we observed from the increased intensity values of the XRD patterns. On the other hand, the average surface (R_a) roughness which was measured using a profilometer for the CdO films is found to be 5.0 nm, when CDO first layers is coated with Si the roughness of CdO/Si reached 10 nm coating CdO/Si with another layers of CdO the roughness of the CdO/Si/CdO decreased to 7.0 nm. The average roughness values are about ~0.6% of the total volume indicating that the roughness does not influence the sample surface significantly. In addition Figure 2a illustrates the energy dispersive X-ray spectra for the CdO/Si/CdO thin films. The spectra indicated the existence of glass (SiO_2:Na_2O:Mg:CaO) , CdO and Au. No other impurities existed in the films. It means that the studied thin films are of high purity. The gold existed because it was coated onto the films surface to prevent electron contamination.

3.3. Optical properties

The effects of Si slabs on the optical properties of CdO thin films are investigated though the measurements of the transmittance (T%) and reflectance (R%) spectra. The measured T% and R% are shown in Figure 2b and 2c, respectively. It is evident from Figure 2b that the stacked layers of CdO are highly transparent. Insertion of the Si slabs between layers of CdO decreases the transmittance values and redshifts the T% spectra. On the other hand, as seen from Figure 2c, the reflectance values of the CdO stacked layers are very low (less than 10%) as it sharply increases with increasing incident light wavelengths (λ) in the range of 200-440 nm. Insertion of the Si slabs between stacked layers of CdO increase the reflectance values and make the increase of R% with increasing λ sharper in a wider range of λ (200-700 nm).
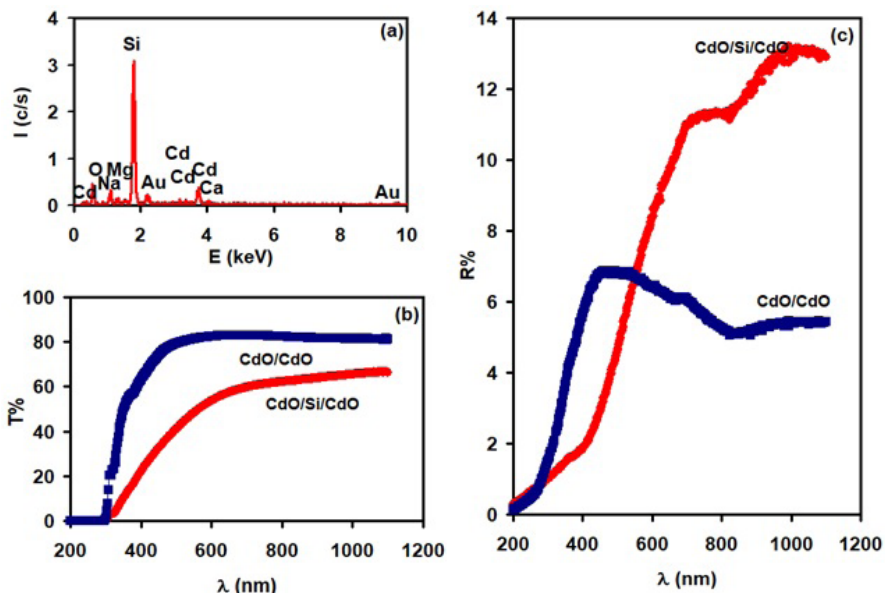

Figure 2. (a) The energy dispersive X-ray analysis for CdO/Si/CdO films. (b)The transmittance and (c) the reflectance spectra for the CdO/CdO and CdO/Si/CdO thin films.

The absorption coefficient (α) spectra are calculated from the measured transmittance and reflectance spectra with the help of the, previously, published equations[8]. The α spectra are presented in Figure 3a that illustrates significant effect of Si slabs on the α values. Namely, the absorption coefficient values increased and the slope of the $\alpha - E$ variations also changed upon insertion of Si slabs between layers of CdO. As it is readable from the inset of Figure 3, the light absorbability ($R_\lambda = \alpha_{CSC} / \alpha_{CC}$) defined as the ratio of the absorption coefficients of CdO in the presence to that in the absence of Si layers are larger than one in the incident light energy range of 1.41-3.63 eV. The higher the incident photon energy, the larger the value of R_λ in that range. A maximum value of 3.03 is read at 3.63 eV. It indicates that in addition to the enhancement of the light absorbability to IR and visible light, the CSC films are more suitable for ultraviolet (UV) signal detection as R_λ has remarkably increased in the UV band. On the other hand, the energy band gap (E_g) is determined with the help of Tauc's equation,

$$\left((\alpha E)^p \propto \left(E - E_g \right) \right). \tag{5}$$

The fittings of Equation 5 in the strong absorption regions of 2.5-4.0 eV and of 2.0-4.0 eV for the CC and CSC samples are illustrated in Figure 3b and 3c. The respective figures reveal direct ($p = 2$) and indirect ($p = 1/2$) energy band gaps of values of 2.20 eV and 1.27 eV. While the stacked layers of CdO exhibit direct allowed transition energy band gaps of values of 2.20 eV and of 3.50 eV, the samples comprising Si in its structure exhibited only one indirect allowed transitions energy band gaps. CdO/CdO samples exhibited an additional indirect ($p = 1/2$) allowed transitions energy band gap of value of 3.50 eV in the highest absorption region. Abnormal engineering in the value (from

2.20 eV to 1.27 eV) and in the nature (from direct to indirect allowed transitions) of energy band gap is achieved via insertion of Si slabs into the structure of CdO. The value of the energy band gap of CC films being 2.20 eV is comparable to the reported as 2.13 eV for undoped CdO thin films[25]. CdO films that are doped with 8.5 wt.% Si exhibited direct allowed energy band gaps of value of 2.38 eV. In contrast to our observation, the energy bands gaps of CdO increased upon increasing Si content in the Si doped CdO samples[25]. Shrinkage in the value of the energy band gap from 2.51 to 1.41 eV upon insertion of indium slabs between layers of Ga_2S_3 was previously reported[8]. Such behavior was assigned to the many-body effects which are known causing shifting up of the valence band and shifting down of the conduction band resulting in the band gap shrinkage[8]. Narrowing the energy band gap upon Si doping was also assigned to the lattice shrinkage caused by the stronger electronegativity of Si (1.80)[32] over that of Cd (1.69).

The band structure studies on CdO have shown that the direct allowed transitions occur between the Γ_{15v} and Γ_{1c} energy bands of the first Brillouin zone within an energy band gap of value of 2.28 eV[33]. The indirect allowed transitions happen with an energy band gap of value of 1.095 eV between Σ_{3v} and Γ_{1c} of the Brillouin zone[33]. Based on the structural analyses, it is possible to think that, the presence of Si slabs between CdO layers created stress and increased the strain that forced the exchange in electronic transition from direct allowed with an energy gap of 2.20 eV to indirect allowed with a band gap of 1.27 eV. It is also worth mentioning that the indirect electronic transitions from the $\Gamma_{25'v}$ state to Δ_{1c} states in silicon[33] results in an energy band gap of value of 1.17 eV, which is also comparable to the observed value of CSC films reported in this work.
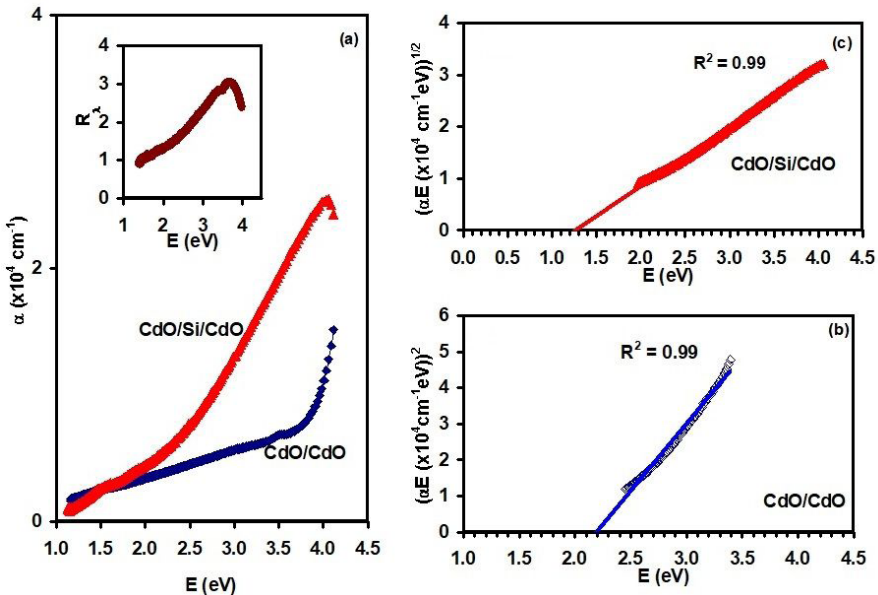

Figure 3. (a) The absorption coefficient, (b) the Tauc's equation fittings for CdO/CdO and (c) the Tauc's equation fittings for CdO/Si/CdO. The inset of (a) illustrates the light absorbability spectra.

Recent studies which are concerned with the optical properties of CdO thin films indicated that doping CdO with Ag result in a decrease the energy band gap with increasing time of Ag ablation[34]. Similar decreasing trend of variations was also observed in $Zn_{1-x}Na_xS$ thin films and was assigned to the variations in the Na content[35]. Copper substitutions into sites of Zn in ZnS also reduced the energy band gap of ZnS[36]. The behavior was assigned to the enrichment of the valance band by more states shared by copper atoms. The increase in the valence band states raises the valance band maxima upward resulting in a decrease in E_g values.

3.4. Dielectric properties

Figure 4a displays the real part of the dielectric (ε_r) spectra for the stacked layers of CdO. The dielectric constant spectra are calculated from the measured transmittance and reflectance spectra with the help of Fresnel's equations for light at normal incidence[9]. Significant enhancement in the dielectric constant value is observed upon insertion of Si layers between stacked layers of CdO. Namely, while the ε_r spectra for CC samples display low values of ~2.1 in most of the spectral range, those of CSC show remarkable increase with decreasing incident light energy. The enhancement in the dielectric constant value exceeds 185% near 1.2 eV. Attempts to find relations between the incident photon energy and dielectric response revealed second degree polynomial with slopes larger by 8 times in CSC samples. While the $\varepsilon_r - E$ variations of the CdO/CdO samples follow the equation $\varepsilon_r = -0.06E^2 + 0.20E + 1.97$, those of CdO/Si/CdO follows the relation, $\varepsilon_r = +0.49E^2 - 3.53E + 6.38$. The static dielectric constant values $\varepsilon_r(0) = \varepsilon_s$ increased from 1.974 to 6.34 upon insertion of Si slabs between layers of CdO. Recalling that the electric susceptibility ($\chi_e = \varepsilon_r - 1$) represents the degree of polarization of a dielectric material in response to an applied electric field, then the enhancements in the dielectric constant response indicate the ability of the CSC samples to store more electromagnetic energy. The quality factor spectra of these stacked layers which are defined as the ratio of the real to the imaginary ($Q = \varepsilon_r / \varepsilon_{im}$) parts of dielectric constants are illustrated in Figure 4b. The quality factor of the CC samples exhibit value of ~40 and is independent of the incident light energy. The insertion of Si slabs increases the dielectric constant value by three times and make it more sensitive to incident light energy. The value of Q reaches 133 at 1.15 eV. This values is acceptable for fabrication of electromagnetic energy storing devices.

Figure 4c show the optical conductivity ($\sigma(\omega) = \frac{\varepsilon_{im}\omega}{2\pi}$; ω: angular frequency) spectra. In general, the conductivity values are highly increases with increasing incident photon energy. The insertion of Si slabs between layers of CdO increases the values of the optical conductivity in the spectral range of 1.9-4.1 eV. As for examples, when the incident photon energy is 3.50 eV, the conductivity increased from 1.91 to 4.38 $(\Omega cm)^{-1}$. The increase in the optical conductivity can be related to the increase in the light absorbability. To give significance for the observed $\sigma(\omega)$, the experimental conductivity spectra are theoretically reproduced with the help of Drude-Lorentz model for optical conduction. In that model, the conductivity is given by[8,9,37],

$$\sigma(\omega) = \sum_{i=1}^{k} \frac{\omega_{pei}^2 \omega^2}{4\pi\tau_i \left(\left(\omega_{ei}^2 - \omega^2\right)^2 + \omega^2 \tau_i^{-2} \right)} . \tag{6}$$

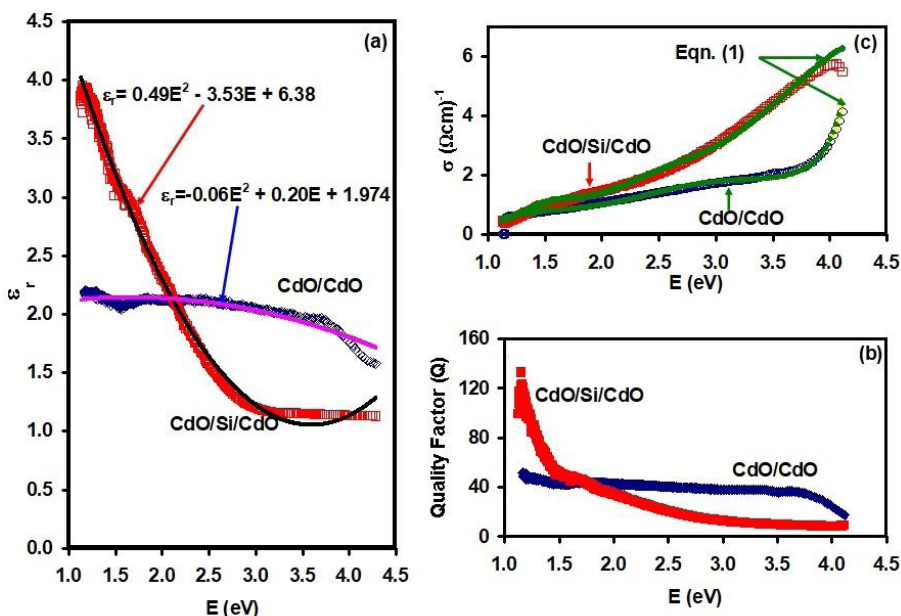$$\omega_{pei} = \sqrt{4\pi n_i e^2 / m^*} \tag{7}$$

Figure 4. (a) The real part of dielectric spectra, (b) the quality factor spectra and (c) the optical conductivity spectra for CdO/CdO and CdO/Si/CdO stacked layers. The green colored black circles in (c) shows the fitting of Drude-Lorentz equation.

$$\tau_i = \frac{\mu_i m^*}{e} \qquad (8)$$

In above equations, ω_{pei}, n_i, m^*, ω_{ei}, τ_i and μ_i are the plasmon frequency, the free charge carrier concentration, the free charge carrier effective mass, the free charge carrier-plasmon reduced frequency, the scattering time at femtosecond level and the drift mobility of holes, respectively. The subscript (i) in the Equations 6, 7 and 8 represents the number of linear oscillators and k is the number of oscillators at which the series terminates. The theoretical solution was executed assuming a charge carrier effective masses of $m^* = 0.33m_o$ [33] for CdO and $m^* = 0.19m_o$ for Si[33]. The reduced effective mass of CSC samples is $m^*_{CSC} = \left[2(m^*_{CdO}{}^{-1}) + m^*_{Si}{}^{-1}\right]^{-1} = 0.088$ m_o. As can be seen in Figure 4c, the experimental data is reproduced assuming the fitting parameters which are shown in Table 1. The solid green circles in the figure assure the good consistency between the experimentally determined and the theoretically calculated values.

The parameters shown in Table 1 indicate that CdO stacked layers exhibit relaxation time at femtosecond level in the range of 0.5-1.5 fs. This value represents the relaxation time of electronic collisions and is the inverse of the electronic friction coefficient ($\gamma \propto \tau^{-1}$). Comparing τ_1 values of the CC and CSC samples for the oscillator which is dominant in the IR range ($E_e = 1.58 \ eV$), one may observe significant increase in the scattering time indicating the reduction in the electronic friction forces upon insertion of Si slabs between layers of CdO. For this oscillator, the silicon layers remarkably enhanced the drift mobility values from 2.13 cm^2/Vs to 15.98 cm^2/Vs. The Si slabs also slightly reduced the plasmon frequency value which is known as the cutoff frequency. Thus, we get the advantage of making the CdO stacked layers more efficient in transporting data as the mobility value is enhanced without significant narrowing the cutoff limit. It is also noticeable that the free charge carrier density decreased from $1.3 \times 10^{18} \ cm^{-3}$ to $3.0 \times 10^{17} \ cm^{-3}$. This change in the number of free charge carriers supports the idea of reduction of dangling bonds of Si atoms upon interaction with Cd vacancies. In other words, some of the free charge carriers in the CC sample shared in completing the bonding of the Si broken bonds. On the other hand, the second oscillator ($E_e = 2.63 \ eV$) is dominant in the visible range of light. It exhibits higher drifts mobility and higher plasmon frequency making the CSC sample attractive for use as signal receivers of gigahertz cutoff frequency. Although the drift mobility values of the strongest ultraviolet oscillator ($E_e = 4.33 \ eV$) do not change upon insertion of Si slabs, the plasmon frequency increased by 173% without much change in the free charge carrier density.

Recent studies on heterojunction devices use CdO as substrates for the photovoltaic. InSe indicated that the plasmon frequency of the CdO/InSe could be altered in the range of 0.10-1.80 GHz. However, the drift mobility of free charge carriers does not exceed 0.35 cm^2/Vs at the highest plasmon frequency value (1.80 GHz)[38]. In the CdO/InSe interfaces, at the oscillator energy which is dominant in the visible range of light ($w_e = 3.6 \times 10^{15} \frac{rad}{s}$; $E_e = 2.36 \ eV$), the free charge carriers exhibited higher drift mobility values than those observed here, but the plasmon frequency is much lower ($w_p = 0.1 \ GHz$). For this reason, inserting thin layers of Si slabs between layers of CdO before using it as substrates may be more suitable and may enhance the performance of the photovoltaic material further. The enhancement in the values of electron mobility upon the participation of Si atoms in the structure of CdO was also observed in Si doped CdO thin films[21,25]. The mobility of these films increased from 8.50 cm^2/Vs to 25.25 cm^2/Vs upon doping CdO with 8.5 wt.% of Si. The mobility increases due to the elimination of electron intersubband scattering[39]. It was shown that the insertion of thin barriers forces confinement of polar phonons that strongly affect the electron mobility[39]. Most of the contributions to the mobility arises from the resonant intersubband scattering of electrons by interface phonons.

Table 1. The optical conductivity parameters for CdO/CdO and CdO/Si/CdO stacked layers.

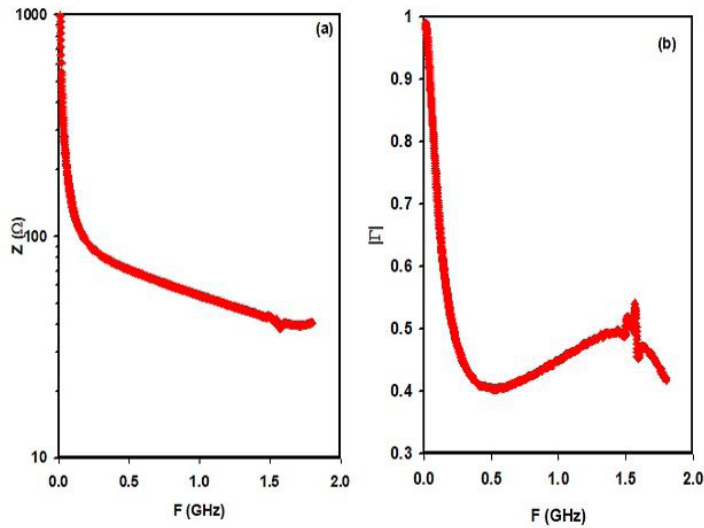| i	CdO/CdO				CdO/Si/CdO			
	1	2	3	4	1	2	3	4
$\tau \ (fs)$	0.4	0.3	0.3	1.5	0.8	0.4	0.4	0.4
$n \ (\times 10^{18} \ cm^{-3})$	1.3	2.2	5.0	5.0	0.3	0.9	1.2	4.0
$\omega_e \ (\times 10^{15} \ Rad/s)$	2.4	4.0	5.5	6.6	2.4	4.0	5.5	6.6
$E_e \ (eV)$	1.58	2.63	3.61	4.33	1.58	2.63	3.61	4.33
$\omega_p \ (GHz)$	1.18	1.53	2.31	2.31	1.00	1.90	2.19	4.01
$\mu \ (cm^2/Vs)$	2.13	1.60	1.60	7.99	15.98	7.99	7.99	7.99

Figure 5. (a) The impedance and (b) the reflection coefficient spectra for the CdO/Si/CdO stacked layers.

3.5. Electrical properties

As practical confirmation to the theoretically estimated plasmonic interactions, the CSC samples were coated onto Yb metal substrate (low work function $\phi = 2.51$ eV) and the top side of the device were contacted with carbon point contacts ($\phi = 5.10$ eV). The work function of CdO is reported to be 3.45 eV[40]. So, the Yb/p-type CSC side forces the formation of Schottky contact and the carbon establishes an ohmic contact. The resulting Yb/CdO/Si/CdO/C devices were subjected to impedance spectroscopy measurements in the frequency domain of 0.01-1.80 GHz. This is the maximum possible range available in our laboratory. The measured impedance (Z) spectra are shown in Figure 5a. It is clear from the figure that the device sharply switches from high impedance to low impedance modes upon frequency increments. Namely, it decreases from 1000 Ω to ~100 Ω as the frequency increases from 0.01 GHz to 0.15 GHz. It then continues decreasing with smoother trends of variation. While the high impedance mode indicated prohibiting signal reception, the low impedance states indicate signal propagation without attenuation[41]. Recalling that the plasma oscillation means the minimum frequency of electromagnetic waves that can travel through the media without attenuation, then the switching from high impedance to low impedance state means that the devices reached the plasmon frequency limit so that signals can propagate. The picture is better presented in Figure 5b. The figure illustrates the magnitude of the reflection coefficient $|\Gamma|$ as function of source frequency (F).

The value of $|\Gamma|$ being 1.0 indicates that all arriving signals at the sample terminals are rejected. According to Figure 5b, the frequency domain is 0.01-0.56 GHz, and the higher the frequency associates with a lower the value of $|\Gamma|$. Once the source frequency reaches 1.56 GHz, $|\Gamma|$ start decreasing with increasing signal frequency reaching a minima at 1.80 GHz. The style of variation of the reflection coefficient spectra means that the CSC samples can be used as active dielectric media for the fabrication of lowpass filters.

It is interesting to compare the effect of Si slabs on the structural, optical and electrical properties of CdO with those of Au metal slabs[42]. The 100 nm thick Si slabs increased the strain stacking faults percentages and defect density in the stacked layers of CdO, while, in contrast, 50 nm thick Au slabs decreased the values of these parameters. However, the narrowing of the energy band gap by the Si slabs is more pronounced than that achieved by the Au slabs. CdO/Si/CdO samples exhibited energy band gaps value of 1.27 eV compared to 1.87 eV which was achieved by Au sandwiching between layers of CdO[42]. In addition, the maximum obtainable drift mobility in the CdO/Au/CdO structure is 10.91 cm²/Vs and is still lower than that obtained for CdO/Si/CdO as 15.98 cm²/Vs. In contrast to what is obtained by Si and Au participation in the structure of CdO, Pb and Cu and Mn doping increased the energy band gap of CdO from 2.20 eV to 2.53 eV[43-45].

The currently reported CdO thin films are compared to the films prepared by physical deposition and chemical deposition techniques[46,47]. CdO thin films grown by the radio frequency magnetron sputtering technique displayed highly uniform nanopyramidal structure. In a good consistency with our observation, the optical analyses on the films grown by the RF technique indicated direct allowed transition energy band gaps of value of 2.2-2.4 eV[46]. On the other hand, CdO thin films, which are prepared by the chemical vapor deposition technique[47], showed amorphous nature of the films in its as grown form. The energy bands gaps of these films varied in the range of 2.42-2.04 eV. Annealing of these films at 623 K resulted in the formation of nanowires of lengths of 2.5-3.0 μm. Although the growth technique strongly affects on the structure and morphology, significant effects on the energy band gap values are not observed.

4. Conclusions

In this current work, the effects of insertion of Si slabs between stacked layers of CdO are investigated. Significant effect on the crystallinity presented by larger grain sizes and

more oriented planes along the (111) direction was observed. In addition, enhancements in the light absorbability, optical conductivity, dielectric constant and in drift mobility values are achieved via insertion of Si slab between layers of CdO. The Si layers forced a change the electronic transitions type from direct to indirect allowed. This change is associated with band gaps shrunk from 2.20 to 1.27 eV. As a practical application of the CdO/Si/CdO interfaces, the impedance spectra that were measured in the frequency domain of 0.01-1.80 GHz revealed the possibility of using this media as low pass filters.

5. Acknowledgements

6. References

1. Avila-Avendano C, Mejia I, Reyes-Banda MG, Lamont JG, Pham C, Caraveo-Frescas JA, et al. Thin-film devices for active pixel sensor schemes enabling high density and large-area sensors. Advanced Materials Technologies. 2021;6(9):2100279.

2. Micha DN, Jakomin R, Kawabata RM, Pires MP, Ponce FA, Souza PL. Nanostructured materials for high efficiency solar cells. In: Fraga MA, Amos D, Sonmezoglu S, Subramaniam V, editors. Sustainable material solutions for solar energy technologies. San Diego: Elsevier; 2021. p. 201-227.

3. Brongersma ML. The road to atomically thin metasurface optics. Nanophotonics. 2021;10(1):643-54.

4. Kalb J, Weller F, Irmler L, Knittel V, Graus P, Boneberg J, et al. Position-controlled laser-induced creation of rutile TiO2 nanostructures. Nanotechnology. 2019;30(33):335302.

5. Li JX, Li YH, Qin ZB, Dong GY. Ultrasound assisted synthesis of a zinc (II) coordination polymer with nano-flower morphology and the use as precursor for zinc (II) oxide nanoparticles. Polyhedron. 2018;155:94-101.

6. Narsimulu D, Vinoth S, Srinadhu ES, Satyanarayana N. Surfactant-free microwave hydrothermal synthesis of SnO2 nanosheets as an anode material for lithium battery applications. Ceram Int. 2018;44(1):201-7.

7. Ding Y, Li S, Tian J, Wang F, Shi Y, Tao X, et al. CNTs/wood composite nanogenerator for producing both steam and electricity. ACS Applied Electronic Materials. 2021;3(12):5287-91.

8. Nazzal EO, Qasrawi AF, Alharbi SR. Engineering the optical and dielectric properties of the Ga2S3/In/Ga2S3 nanosandwiches via indium layer thickness. Plasmonics. 2018;13(3):1049-56.

9. Qasrawi AF, Taleb MF. Effect of Y, Au and YAu nanosandwiching on the structural, optical and dielectric properties of ZnSe thin films. Chalcogenide Lett. 2019;16(3):95-105.

10. Wang C, Li Q, Wang J, Zhang L, Zhao F, Dong F. High quality ZnS/Au/ZnS transparent conductive tri-layer films deposited by pulsed laser deposition. Opt Spectrosc. 2016;121(1):68-71.

11. Goktas S, Goktas A. A comparative study on recent progress in efficient ZnO based nanocomposite and heterojunction photocatalysts: a review. J Alloys Compd. 2021;863:158734.

12. Soylu M, Kader HS. Photodiode based on CdO thin films as electron transport layer. J Electron Mater. 2016;45(11):5756-63.

13. Lee J, Kwon J, Seo D, Na J, Park S, Lee HJ, et al. Plasma-doped si nanosheets for transistor and p−n junction application. ACS Appl Mater Interfaces. 2019;11(45):42512-9.

14. Le K, Wang Z, Wang F, Wang Q, Shao Q, Murugadoss V, et al. Sandwich-like NiCo layered double hydroxide/reduced graphene oxide nanocomposite cathodes for high energy density asymmetric supercapacitors. Dalton Trans. 2019;48(16):5193-202.

15. Wang PP, Zhang YX, Fan XY, Zhong JX, Huang K. Synthesis of Si nanosheets by using Sodium Chloride as template for high-performance lithium-ion battery anode material. J Power Sources. 2018;379:20-5.

16. Salih AT, Najim AA, Muhi MA, Gbashi KR. Single-material multilayer ZnS as anti-reflective coating for solar cell applications. Opt Commun. 2017;388:84-9.

17. Adam AM, Elsehly EM, Ataalla M, El-Khouly A, Nafady A, Diab AK. Preparation and thermoelectric power properties of highly doped p-type Sb2Te3 thin films. Physica E. 2021;127:114505.

18. Zhang D, Xie Q, Cai H, Zhang X, Li S, Han G, et al. Synthesis and separation property of flower-like Cd (OH) 2 microstructures via a simple solution route. Appl Surf Sci. 2010;256(21):6224-7.

19. Bulakhe RN, Lokhande CD. Chemically deposited cubic structured CdO thin films: room temperature. In: AIP Conference Proceedings; 2013 Jun 3. New York: American Institute of Physics; 2013. p. 503-504.

20. Sebastian PJ, Calixto ME. Porous CdS: CdO composite structure formed by screen printing and sintering of CdS in air. Thin Solid Films. 2000;360(1-2):128-32.

21. Dakhel AA. Structural and optoelectronic properties of Zn-incorporated CdO films prepared by sol–gel method. J Alloys Compd. 2012;539:26-31.

22. Ilkhechi NN, Aghjehkohal AR. TanourAghaj EF, Mozammel M. Enhanced optical and hydrophilic properties of Si and Cd co-doped TiO2 thin films. J Mater Sci Mater Electron. 2017;28(6):4598-605.

23. Xiao Y, Qi Y, Wang X, Wang X, Zhang F, Li C. Visible-light-responsive 2D cadmium–organic framework single crystals with dual functions of water reduction and oxidation. Adv Mater. 2018;30(44):1803401.

24. Zhang Y, Zhang J, Jiang J, Hou D, Zhang J. The effect of water molecules on the structure, dynamics, and mechanical properties of sodium aluminosilicate hydrate (NASH) gel: a molecular dynamics study. Constr Build Mater. 2018;193:491-500.

25. Dakhel AA. Impact of silicon doping on the properties of transparent conducting CdO thin films. Silicon. 2019;11(1):525-32.

26. Dakhel AA. Electro-optical properties of hydrogenated Si-doped CdO. J Electron Mater. 2018;47(1):773-7.

27. Marceau RK. Atomic-scale analysis of light alloys using atom probe tomography. Mater Sci Technol. 2016;32(3):209-19.

28. Maity R, Chattopadhyay KK. Synthesis and characterization of aluminum-doped CdO thin films by sol–gel process. Sol Energy Mater Sol Cells. 2006;90(5):597-606.

29. Mikailzade F, Türkan H, Önal F, Zarbali M, Göktaş A, Tumbul A. Structural and magnetic properties of polycrystalline Zn1−xMnxO films synthesized on glass and p-type Si substrates using Sol–Gel technique. Appl Phys, A Mater Sci Process. 2021;127(6):1-8.

30. Goktas A, Modanlı S, Tumbul A, Kilic A. Facile synthesis and characterization of ZnO, ZnO: Co, and ZnO/ZnO: Co nano rod-like homojunction thin films: Role of crystallite/grain size and microstrain in photocatalytic performance. J Alloys Compd. 2022;893:162334.

31. Gencer H, Goktas A, Gunes M, Mutlu HI, Atalay S. Electrical transport and magnetoresistance properties of La 0.67 Ca 0.33 MnO 3 film coated on pyrex glass substrate. Int J Mod Phys B. 2008;22(05):497-506.

32. Li T, Ding D. Enhanced photoelectrochemical water splitting performance of Ni/Si-doped TiO2 photoanode fabricated through electrochemical reduction in aqueous solutions. J Electrochem Soc. 2020;167(6):066514.

33. Madelung O. Semiconductors: data handbook, Marbur: Springer Science & Business Media; 2012. pp. 218-220.

34. Mostafa AM, Mwafy EA. Laser-assisted for preparation Ag/CdO nanocomposite thin film: structural and optical study. Opt Mater. 2020;107:110124.

35. Goktas A, Tumbul A, Aslan F. A new approach to growth of chemically depositable different ZnS nanostructures. J Sol-Gel Sci Technol. 2019;90(3):487-97.

36. Goktas A. Role of simultaneous substitution of Cu2+ and Mn2+ in ZnS thin films: defects-induced enhanced room temperature ferromagnetism and photoluminescence. Physica E. 2020;117:113828.

37. Pankove JI. Optical processes in semiconductors. 1st ed. New Jersey: Courier Corporation; 1975. pp. 3-41.

38. AlGarni SE, Qasrawi AF. Nonlinear optical performance of CdO/InSe interfaces. Phys Scr. 2020;95(6):065801.

39. Pozela J, Namajūnas A, Pozela K, Jucien V. Polar optical phonon confinement and electron mobility in quantum wells. Physica E. 1999;5(1-2):108-16.

40. Bagal VS, Patil GP, Deore AB, Suryawanshi SR, Late DJ, More MA, et al. Surface modification of aligned CdO nanosheets and their enhanced field emission properties. RSC Advances. 2016;6(47):41261-7.

41. Lee WH, Chen H, Tang CW, Su CY, Lei R. High performance packaging with multilayer ceramic antenna switch module for wireless communication. In: Proceedings of the 4th International Symposium on Electronic Materials and Packaging; 2002 Dec 4. Piscataway: IEEE; 2002. p. 403-408.

42. Alharbi SR, Qasrawi AF. Effects of Au nanoslabs on the performance of CdO thin films designed for optoelectronic applications. Physica E. 2021;125:114386.

43. Güney H. The structural, morphological, optical and electrical properties of Pb doped CdO thin films grown by spray method. Vacuum. 2019;159:261-8.

44. Gupta RK, Yakuphanoglu F, Amanullah FM. Band gap engineering of nanostructure Cu doped CdO films. Physica E. 2011;43(9):1666-8.

45. Alahmed ZA, Albrithen HA, Al-Ghamdi AA, Yakuphanoglu F. Optical band gap controlling of nanostructure Mn doped CdO thin films prepared by sol–gel spin coating method. Optik. 2015;126(5):575-7.

46. Sakthivel P, Murugan R, Asaithambi S, Karuppaiah M, Rajendran S, Ravi G. Radio frequency magnetron sputtered CdO thin films for optoelectronic applications. J Phys Chem Solids. 2019;126:1-10.

47. Dhawale DS, More AM, Latthe SS, Rajpure KY, Lokhande CD. Room temperature synthesis and characterization of CdO nanowires by chemical bath deposition (CBD) method. Appl Surf Sci. 2008;254(11):3269-73.